Journal of Materials Chemistry A

Accepted Manuscript

ROYAL SOCIETY OF CHEMISTRY

www.rsc.org/materialsA

Vapor Phase Conversion of PbI_2 to $CH_3NH_3PbI_3$: Spectroscopic Evidence for Formation of an Intermediate Phase

Sagar Motilal Jain[1]*, Bertrand Philippe[2], Erik M. J. Johansson[1], Byung-wook Park[1], Håkan Rensmo[2], Tomas Edvinsson[3], Gerrit Boschloo[1]*

[1]*Uppsala University, Department of Chemistry-Ångström Laboratory, Physical Chemistry, Box 523, SE 751 20 Uppsala, Sweden*

[2]*Uppsala University, Department of Physics and Astronomy, Molecular and Condensed Matter Physics, Box 516, SE 751 20 Uppsala, Sweden*

[3]*Department of Engineering Sciences – Solid State Physics, Uppsala University, Box 534, SE 751 21 Uppsala, Sweden*

ABSTRACT

The formation of $CH_3NH_3PbI_3$ ($MAPbI_3$) from its precursors is probably the most significant step in the control of the quality of this semiconductor perovskite material, which is highly promising for photovoltaic applications. Here we investigated the transformation of spin coated PbI_2 films to $MAPbI_3$ using a reaction with MAI in vapor phase, referred to as vapor assisted solution process (VASP). The presence of a mesoporous TiO_2 scaffold on the substrate was found to speed up reaction and led to complete conversion of PbI_2, while reaction on glass substrates was slower, with some PbI_2 remaining even after prolonged reaction time.

Based on data from UV-visible spectroscopy, Raman spectroscopy, X-ray diffraction and X-ray photoelectron spectroscopy, the formation of an X-Ray amorphous intermediate phase is proposed, which is identified by an increasing absorption from 650 to 500 nm in the absorption spectrum. This feature disappears upon long reaction times for films on planar substrates, but persists for films on

mesoporous TiO_2. Poor solar cell performance of planar VASP prepared devices was ascribed to PbI_2 remaining in the film, forming a barrier between the perovskite layer and the compact TiO_2/FTO contact. Good performance, with efficiencies up to 13.3%, was obtained for VASP prepared devices on mesoporous TiO_2.

KEYWORDS: Organic inorganic lead halide perovskite, Vapor assisted reaction, X-ray diffraction spectroscopy, Optical spectroscopy, Resonance Raman etc.

INTRODUCTION

Despite the rapid progress in the perovskite solar cell device performance, the structural and electronic properties of hybrid lead halide perovskites are far from being fully understood. Lead halide perovskite materials exhibit many interesting physico-chemical properties, such as high absorption coefficient, the possibility to tune its band gap from 1.4 to 3.0 eV, and suitable electron and hole transport properties, which make this material very well suited for photovoltaic devices. This is reflected by the remarkable increase of power conversion efficiencies (PCE) of perovskite - based solar cells in the last five years, from 3.8 % to 17.3 % for methylammonium lead triiodide ($MAPbI_3$) based perovskite [1], [2], [3], [4].

Many of the physical properties of the perovskite depend crucially on small distortions in the structure, such as the tilting of the PbI_6^{4-} octahedron driven by the organic cations, and displacement of the cations out of the center of their polyhedron [5].

It is well recognized that the crystallite quality of perovskite films plays an important role in achieving high efficiency solar cells. Therefore, the development of optimized perovskite preparation methods is an active area of the research. Methods commonly used to prepare perovskite films can be divided into solution-based and vapor deposition methods. Solution-based methods are often based on spin coating of the precursors. However, owing to the relatively fast crystallization of perovskite materials and the lack of good solvents for the precursors, spin coated films may have an incomplete surface coverage with pinholes or an island structure [6], [7]. A two-step solution based method, in which spin-coated

PbI_2 films are dipped into a solution of CH_3NH_3I (MAI) in isopropanol gave promising results, [1] but this method is very sensitive to the concentration of the organic halide, the temperature, and the reaction time, resulting in difficulty to control the final quality of the perovskite films. This method involves rinsing with isopropanol, that can partially dissolve perovskite material and convert it back to PbI_2 [8], [9].

Snaith et al. [4] and Chen at al. [11] have produced high quality $CH_3NH_3PbI_{3-x}Cl_x$ films by thermal vapor co-deposition of MAI and $PbCl_2$ and sublimation of $PbCl_2$ and MAI in later case respectively. However; these methods are more energy consuming and requires an expensive high vacuum set-ups.

Careful controlled synthesis of perovskite material at atomic/molecular level can be achieved by controlling many factors *e.g.* solvents, crystallization, post-annealing temperature and reaction time [6], [10], [12], [13]. In this work, a vapor assisted solution process (VASP) for $MAPbI_3$ synthesis is used, as introduced by Y. Yang et al.[15]. This two-step method combines solution based deposition of PbI_2 with a vapor-phase reaction of MAI at atmospheric pressure (N_2 atmosphere, 150°C). This methodology enables good control of the rate of $MAPbI_3$ crystal growth and enabled us to study partial conversion and intermediate stages during synthesis. The reaction mechanism in the VASP process is as follows:

$$PbI_2\ (s) + CH_3NH_3I\ (s) \rightarrow PbI_2 + CH_3NH_2\ (g) + HI\ (g) \rightarrow\ CH_3NH_3PbI_3\ (s)$$

It is expected that the small gas phase methylamine (CH_3NH_2) molecules and hydrogen iodide (HI) can intercalate in the sheet-like PbI_2 structure with relative ease.

Using a simple calculation, it can be estimated that the volume of the solid ($PbI_2 \rightarrow CH_3NH_3PbI_3$) during this reaction increases by 100%:

$$\frac{V_{MAPbI_3}}{V_{PbI_2}} = \frac{\rho_{PbI_2}}{\rho_{MAPbI_3}} \times \frac{M_{MAPbI_3}}{M_{PbI_2}},$$

Where, V is the volume of the material, ρ is the density (4.16 g cm^{-3} for $MAPbI_3$ [16], 6.16 g cm^{-3} for PbI_2) and M the molecular formula weight. The mechanism of formation of perovskite from PbI_2 and MAI is not fully understood and few studies of the confinement effect inhibited by inorganic PbI_6 as well by the volume confinement within the TiO_2 scaffold has so far been reported [1]. The VASP technique has so far only been used for the preparation of thin film devices with planar structure, but here we show for the first time that it also can be a promising route for the preparation of $MAPbI_3$ on mesoporous TiO_2 scaffold.

Here, we investigated the conversion of PbI_2 thin films to $MAPbI_3$ in detail and found evidence for the formation of an intermediate phase that can partially remain in the end product. The presence of an intermediate phase was reported before for solution-processed $MAPbI_3$ when external additives such as NH_4Cl [17] or and $CaCl_2$ [18] were present in the precursor solution.

RESULTS AND DISCUSSION

X-Ray Diffraction :

Spin coated PbI_2 thin films (~ 500 nm) on plain glass substrates and on glass with ~ 350 nm mesoporous (ms) TiO_2 scaffold layer were exposed to MAI vapors at 150°C during different periods of time. The formation of $MAPbI_3$ perovskite was followed using X-ray diffraction (XRD), see Figure 1. The PbI_2 films (0 min. reaction time) show a main peak at 12.5° (2θ), which is characteristic of the PbI_2 (001) hexagonal crystal structure. The Scherrer equation was used to estimate an average crystallite size from broadening of the main XRD peaks (S3) [19], [20]. The grain size of PbI_2 was found to be 34.4 nm on plain glass and 14.4 nm on glass/ms-TiO_2.

For the samples on glass, the intensity of the main PbI_2 peak increased after 10 minutes reaction time, which is attributed to an increase in crystallinity and grain size (≈ 40 nm) in the film, caused by the thermal treatment.

After 10 minutes reaction there is clear evidence of the formation of $MAPbI_3$ in both types of sample from the appearance of XRD peaks at 2θ : 14.12 (110), 28.41 (220), 31.85 (310), 43.19° (330), representing formation of tetragonal $MAPbI_3$ crystals. After 30 minutes, reaction appears complete for samples on ms-TiO_2, as no PbI_2 peaks are visible, while for samples on glass, the main XRD peaks of $MAPbI_3$ and PbI_2 are similar in intensity.

After 60 minutes, the PbI_2 peak at 12.5° has almost disappeared form the samples on glass, but a small shoulder is still remaining, see Fig. 1 (a) and S2 (a) in supporting information. The intensity of the main $MAPbI_3$ XRD peak did not change significantly, but the maximum is found at 2θ of 13.9°. This suggests a change in the most preferred orientation from (110) (predicted at 14.2) to (002) (at 13.9°). These close-lying XRD peaks prevent accurate determination of the perovskite grain size. Further increase in the reaction time beyond 60 minutes did not lead to full conversion of PbI_2 as the small shoulder peak at 12.5° was persistent (Supporting information figure S2 (a) and (b)).

(Figure 1)

Scanning electron microscopy Scanning electron microscopy (SEM) was used to study the surface morphology of the thin films during the conversion process from PbI_2 to $MAPbI_3$, see Figure 2. For this purpose, the samples were prepared on conducting fluorine-doped tinoxide (FTO)-coated glass and on FTO with mesoporous TiO_2 scaffold layer. PbI_2 films on FTO have a very smooth surface morphology, showing hexagonal grains and appear to be quite dense (Figure 2a). In comparison, PbI_2 films on mesoporous TiO_2 scaffold layers appear much rougher and porous (Figure 2b). Using higher

magnification, it can be seen that in this case that the PbI_2 layer is comprised of elongated grains that are significantly smaller than those in films without scaffold, in agreement with the XRD results.

After 10 minutes, significant morphological changes are observed in both cases. In the films on FTO glass, isolated perovskite crystals appear at the surface within the PbI_2 matrix. For films on ms-TiO_2, the small elongated grains transform to larger, more rectangular grains. Upon longer reaction times, the crystals grow and fuse together to give bigger $MAPbI_3$ crystals.

The formation of bigger $MAPbI_3$ crystals after 30, 45 and 60 minutes is likely the result of the thermodynamically driven Ostwald ripening process in which the smaller $MAPbI_3$ crystals dissolve and re-deposit forming larger $MAPbI_3$ crystals [21].

In a recent study, methylamine gas was shown to have a profound effect on recrystallization of the hybrid perovskite material [22]. The grain/crystal size constantly increases in both cases as function of the reaction time, in agreement with the XRD results. The increase of $MAPbI_3$ surface crystal size is from about 200 nm to ~ 1500 nm (1.5 μm) upon increasing the reaction time from 10 to 60 minutes for $MAPbI_3$ prepared on FTO or from 10 to 30 minutes reaction time for FTO/ms-TiO_2. This leads to a reduction in the number of the grain boundaries.

(Figure 2)

UV-Visible Spectroscopy The transformation of PbI_2 to $MAPbI_3$ by vapor phase reaction with MAI was also probed by UV-visible spectroscopy, using thin films on plain glass and on mesoporous TiO_2/ glass, see Figure 3.

(Figure 3)

The UV-visible spectra of the initial PbI_2 films show an absorption onset at 515 nm (2.4 eV), with an excitonic peak at 495 nm, and a further absorption that increases towards the UV- region. The absorption features at wavelengths higher than 515 nm are attributed to interference patterns [14], indicating that the spin coated PbI_2 layer has a very smooth surface and uniform thickness. After 10 minutes of reaction, a clear absorption edge appears at about 780 nm, which is attributed to formation of $MAPbI_3$ perovskite. The absorption onset does not change with reaction time, and corresponds to a band gap of 1.59 eV. This is similar to what has been reported for other thin film preparations [23], [24] but larger than the value 1.51 eV reported for single crystalline $MAPbI_3$ [25], [26].

The PbI_2 feature below 525 nm is still clearly visible after 10 minutes of reaction time, but is smaller than that in the unreacted film. This demonstrates partial conversion of PbI_2 to perovskite, estimated to be about 50% in both types of film, based on the decrease of the PbI_2 peak. The evolution of these spectra with reaction time is also reflected in a change of color in the samples, which turns from yellow (crystalline PbI_2) to dark brown ($MAPbI_3$), as shown in the *inset* pictures of Figure 3. After 30 minutes for samples on glass, the $MAPbI_3$ absorption strongly increases, while a weak feature of PbI_2 is still detected. Notably, the whole spectrum is effectively shifted upwards due to light scattering effects caused by the formation of large perovskite crystals. A similar upward shift is observed for $MAPbI_3$ prepared on glass/mesoscopic TiO_2. This feature is most apparent at wavelengths higher than 800 nm, where no light absorption by $MAPbI_3$ occurs.

After 30 minutes reaction time the absorption spectrum shows a strong shoulder at about 560 nm (an increase of absorbance in the range from 650 down to 500 nm, see Figure 3a. Interestingly, this absorption largely disappears upon prolonged reaction time for the films on glass. For 60 minute reaction time the absorption spectrum is much more flat in the 350 - 750 nm region. A similar flat absorbance has been reported for bulk crystalline $MAPbI_3$ [23] and single crystalline $MAPbI_3$ [25], [26]. In contrast, the absorbance increase in the 650 to 500 nm range remains in films prepared on ms-TiO_2.

(Figure 4)

Photoluminescence Spectroscopy Steady-state photoluminescence (PL) measurements were performed on the samples prepared on glass, see Fig. 4. PbI_2 films shows an emission peak at 525 nm (2.39 eV), while the PL maximum for $MAPbI_3$ was found in the range 775 to 781 nm (1.59 eV), in good agreement with the optical band gaps determined from UV-vis absorption spectra (Fig. 3a). For comparison, single crystalline $MAPbI_3$ has an emission peak at 820 nm (1.51 eV) [25], [26]. The PL intensity of PbI_2 decreases with reaction time and disappears after ca. 30 minute, demonstrating the conversion of this material to $MAPbI_3$ and / or energy transfer from excited PbI_2 that is remaining to $MAPbI_3$ (Fig. 4).

The $MAPbI_3$ - based PL intensity show a marked strong maximum after 10 minutes of reaction time the $MAPbI_3$ emission is very high, with a maximum at 775 nm. We attribute to a confinement effect caused by small perovskite crystals embedded in a PbI_2 matrix, which passivates the crystal surface. Energy transfer from excited PbI_2 to$MAPbI_3$ nanocrystals can explain the strong emission found. The PL intensity drops at 30 minutes, but follows increasing trend at longer times, due to increase of $MAPbI_3$ crystallite size and reduction of grain boundaries. After 60 minutes of reaction time the PL emission maximum is slightly shifted to 781 nm. This red shift can be an indication of the increase of the $MAPbI_3$ crystal size [27].

(Figure 5)

Raman spectroscopy The conversion of PbI_2 to $MAPbI_3$ on plain glass and mesoporous TiO_2 scaffold substrates was also investigated using Raman spectroscopy. Some distinct differences were observed between the two types of samples, see Figure 5. Noticeably, the Raman spectrum for the $MAPbI_3$

sample on glass-TiO_2 scaffold after 20 and 30 minutes reaction time shows increased signal from the TiO_2 anatase. Raman scattering revealing that the films are creeping down in the mesosopic structure exposing more of the TiO_2 in the Raman cross section.

The symmetry of an unperturbed 6-coordinated lead, PbI_6 as an isolated cluster belongs to the O_h group and generates three Raman active bands [28] and any perturbation caused by intercalating cations will split the degenerated vibrations and shifts the Raman peaks to higher wavenumbers. Performing DFT calculations using the hybrid B3LYP functional and the scalar relativistic Stuttgart-Dresden basis set with and without a cationic environment, we see a broadening due to split of degeneracy of the vibration modes and shift to higher wavenumbers as summarized in Figure 6. Also new features arising from the cation libration turn up at 150 cm^{-1} in good agreement with previous studies on a cluster level [28] and in periodic calculations [29].

In periodic calculations there is also a band seen at 300 cm^{-1} [29] assigned to the motion of MA. The lack of the band on a cluster level thus indicate that this motion is related to the combination of MA modes in the full periodic system and can then correspond to the frequency doubled band of the 150 cm^{-1} band.

(Figure 6)

The consumption of anionic PbI_2 is thus accompanied by an increased intercalation of MA^+ cations that lead to the shift of the experimental Raman peak from 65 to 80 cm^{-1} that can be assigned to the double degenerated transition from B to B´ mode from linear response DFT calculations and 83 to 94 cm^{-1} for mode C into mode C´. These modes are connected to the symmetric and asymmetric breathing mode of the PbI_6 octahedron as illustrated Figure 5 (a), (b). In addition the Pb—I breathing mode at 94 cm^{-1} that can be assigned to mode C´, disappears with reaction time while these changes are happening the perovskite band at 145 cm^{-1} (from MA motion in $MAPbI_3$) grows as an indication of intercalation of

MA into the PbI_2 framework. This is also supported by the linear response DFT which show additional combination band at 143 cm^{-1} (MA^+ rotation), 149, 154 cm^{-1} (MA^+ wagging), and 156 cm^{-1} (MA^+- MA^+ symmetric stretch) for the small cluster and slightly shifted (~5 cm^{-1}) to higher wavenumbers for the larger $(MAPbI_3)_4$ cluster. The vibrations at 140-160 cm^{-1} therefore contains more detailed information of the MA^+ intercalation in the PbI_2 to form the fully crystalline perovskite. The combined look at the XRD and the broadening of the absorption spectra as amorphous, intermediate phase of perovskite. (Figure 3 (a), (b)) thus intermediate phase of the material for which Raman spectroscopy of the shift of mode A, B, and C as well as the new MA bands can give more details of the MA^+ environment and thus the intercalation process (Figure 5).

The flat shaped spectral UV-visible band after 60 minutes of reaction time on glass substrate (Figure 3(a)) (absorbance shift ≈ 820 nm), belongs to the crystalline $MAPbI_3$ is in well agreement as is reported in literature [23] Also, we see from the Raman spectroscopy the disappearance of the unperturbed Pb—I breathing mode as a further indication of formation of $MAPbI_3$ crystalline phase, although at this step we notice remnant of PbI_2 (shoulder peak at 12.5 θ) presence from XRD patterns and Raman spectroscopy presence of perturbed Pb—I breathing modes and bands associated with the MA motion. Raman spectroscopy also reveals a band at 270-300 cm^{-1} for the fully crystalline perovskite in the TiO_2 scaffold that is interesting to compare with single crystal data. Raman data for single crystal $MAPbI_3$ is not yet published to our knowledge, but comparison with tetragonal phase of $MAPbCl_3$ revealing a band centered at 318 cm^{-1} [30] Where exchange to the heavier iodide should shift this mode to lower wavenumbers and could possibly be the same mode we observe at 270 - 300 cm^{-1}. As mentioned above, periodic calculations [29] give a band at around 300 cm^{-1}, lacking in cluster calculations indicating that this band may be ascribed to higher ordering of the MA cations in the fully periodic system and thus a frequency doubled 140 - 150 cm^{-1} band.

X-Ray photoelectron spectroscopy To get further insights into the VASP reaction, X-ray photoelectron spectroscopy (XPS) was carried out on the PbI_2 film deposited on FTO substrates as well as after reaction for 10, 30, 45 and 60 minutes with MAI. The overview spectra of these samples are presented in Figure S5. and the characteristic core level peak of PbI_2 and $MAPbI_3$ materials (Pb, I, N and C) are clearly observed. The overview spectra confirm that a full surface covering of the TiO_2/FTO substrate is achieved as no Ti or Sn core level peaks can be detected. In addition, it can be noticed that no additional elements such as sulfur or fluorine originated by the use of DMF : DMSO solvents were detected. Further information on the transition from PbI_2 to $MAPbI_3$ can be obtained looking at some specific core level peaks presented in Figure 7a-c.

(Figure 7)

The I4d and Pb5d core level spectra are presented in Fig. 7a. The advantage by using these specific core levels rather than the commonly used I3d and Pb4f is that information from iodine and lead are displayed in the same spectral range and the relative intensity ratio between Pb and I can be measured with a specific probe depth and in a more accurate way as we avoid extra incertitude due to data treatment such as two normalization steps instead of one in this case.

I4d and Pb5d core peak spectra have two components each due to the spin orbit splitting into $d_{5/2}$ and $d_{3/2}$. The measured splitting is 2.65 eV for Pb5d and 1.7 eV for I4d and in the following discussion the binding energy mentioned. We will only refer to the $d_{5/2}$ components. The spectra were intensity normalized to the $Pb5d_{5/2}$ core level peak, which allows us to easily follow the evolution of the stoichiometry as a function of the reaction time with MAI by directly looking at the evolution of the I4d core level peak. The I/Pb ratio before reaction with MAI was estimated to be ~ 1.9 in very good agreement with the stoichiometry of PbI_2 [31].

When MAI is introduced, the I/Pb ratio is increasing and reaches 3.0 after 60 min as expected for the perovskite materials. The intermediate steps have a ratio ~ 2.5-2.6 corresponding to a mixture of PbI_2 and $MAPbI_3$. It is difficult to properly curve fit the Pb5d and I4d spectra with two components assigned to the precursor and the perovskite in the intermediate step, as PbI_2 and $MAPbI_3$ have signature very close in binding energy. Nevertheless, we can remark that the full width at half maximum (fwhm) of the overall $Pb5d_{5/2}$ core level peak is increasing from 0 min to 30 minutes (from 0.84 to 0.91eV) and decreasing from 30 min to 60 min (from 0.91 to 0.80 eV) confirming the transition from PbI_2 to $MAPbI_3$ via a phase where both materials are coexisting in perfect agreement with the XRD results previously presented. A similar evolution is observed for the FWHM of the $I4d_{5/2}$ core level.

After 60 minutes reaction time, the I/Pb ratio and the low FWHM values measured suggested that no PbI_2 remains at the surface of the sample while it was still present in trace by XRD. This difference is explained by the very surface sensitivity of the XPS where only first tens nanometer are probed. This difference confirms that remaining PbI_2 is located at the interface with the substrate rather than at the surface of the sample as represented in a cartoon in Figure 10 (c).

The transition from PbI_2 to $MAPbI_3$ can also be monitored by the N1s and C1s core level peak presented in Fig. 7b and c, respectively. These spectra have been intensity normalized to $Pb7f_{7/2}$. No nitrogen peak is observed before reaction with MAI. After 10 min., a peak at 402.6 eV appears and increases in intensity as the reaction time increase. This single peak is assigned to the nitrogen present in $CH_3\mathbf{N}H_3PbI_3$. The C 1s core level of PbI_2 is composed of a main peak at 285 eV attributed to common surface contamination species. Upon reaction with MAI, a new peak at 286.5 eV appears and increases in intensity in a similar way that the N1s signal. This new peak is assigned to the methyl group present in the perovskite materials i.e. $\mathbf{C}H_3NH_3PbI_3$.

(Figure 8)

The valence spectra of the PbI_2 layer and after a reaction time of 10, 30, 45 and 60 min with MAI are presented in Figure 8. DFT calculations performed in previous works [32] show that the main structure in 1 - 6 eV energy range is mainly due to the DOS of iodine. The DOS of lead contributed as well in the feature observed at 4 - 6 eV and to the peak at 9 - 10 eV. When forming the perovskite, we can see that this last structure is unchanged while the intensity of the main structure located around 1 - 6 eV increases and the shoulder at 4 - 6 eV is strongly attenuated as a direct results from the iodine increased content. The overall signature is similar to the one experimentally reported to the $MAPbI_3$ [33].

Another interesting point is the valence edge of the perovskite materials and PbI_2 roughly located at the same energy. This similarity clearly shows that the different energy band gap between PbI_2 (~2.3 eV) and $MAPbI_3$ (~1.55 eV) is due to difference in the conduction band alignment and the methyl ammonium seems to lower the conduction band level compared to pure PbI_2.

Discussion of material characterization: Combining all results shown above leads to several findings: during the VASP process, gas phase methylamine and hydrogen iodide formed from the methylammonium iodide salt intercalate into the PbI_2 structure, and eventually reacts to form $MAPbI_3$ perovskite. XRD shows that crystalline PbI_2 does not completely disappear in films on glass. Since XPS gives evidence for full conversion at the surface of the film after 60 minutes reaction (an I/Pb ratio of 3), it is most likely that the remaining PbI_2 is present near the glass substrate. Another interesting observation from XPS is that in the period 10 to 45 minutes reaction the I/Pb ratio at the surface of the film is about 2.5. Since the surface is directly exposed to CH_3NH_2 and HI vapors, full conversion the $MAPbI_3$ would be expected there. Instead, the I/Pb ratio remains almost constant in this period. This may suggest formation of an intermediate phase with the stoichiometry $(MAI)_{0.5}(PbI_2)$. This is also supported by the N1s peak in XPS measurements, that are found the double from 30, 45 minute reaction time to 60 minutes.

In addition, experimental resonance Raman spectroscopy data shows a gradual shift of Pb-I vibrations with reaction time, suggesting the intercalation of MA^+ inside PbI_6^{4-}, as supported by DFT calculations. This further suggests the formation of an intermediate phase.

Crystalline PbI_2 in films on mesoporous TiO_2 substrates are more rapidly and fully converted, as follows from the XRD and resonance Raman spectroscopy (Fig. 1b and Fig. 5b). This is perhaps surprising since part of the PbI_2 is present inside the porous TiO_2 structure, where access of the vapor could be more limited. The opposite is true, the pores are in fact only partially filled with PbI_2 in the spin coated process (≈ 50 %) and access and reaction of the vapors in this type of film is therefore more rapid. Since there is a 100 % increase in volume upon reaction, full conversion is only possible in partially filled pores.

Perhaps the most striking feature in this study is the development of the absorption spectrum as function of VASP reaction time: for the samples on glass, the 10 to 45 minute samples show an increasing absorption in the 650 to 500 nm range, while the absorption is essentially flat after 60 minutes reaction time (Fig. 3a). Tentatively, we ascribe the 650 to 500 nm absorption to an intermediate $(MAI)_{0.5}(PbI_2)$ phase, with the argument that the absorption can be considered a red-shifted and broadened PbI_2-like absorption.

The proposed intermediate phase agrees with previous studies that state that only a fraction of the $MAPbI_3$ perovskite is present in a crystalline state in case of solution process films on mesoporous substrates [1]. Specifically, analysis of X-ray scattering of $MAPbI_3$ in ms-TiO_2 suggested the presence of 70% disordered or amorphous phases [23]. Very recently, M. J. Heben and co-workers found evidence for the presence of an intermediate phase between PbI_2 polytype and $MAPbI_3$ perovskite [34].

(Figure 9)

Solar cell characterization Planar $MAPbI_3$ solar cell devices were made using films with different reaction time (different degree of $MAPbI_3$ conversion) on FTO substrates with a compact layer of TiO_2 prepared by spray pyrolysis. In addition, devices with an additional mesoporous TiO_2 layer were prepared with 30 minutes reaction time, which corresponds to full conversion for these films. Spiro-MeOTAD was used as the p-type contact for the solar cells. The crossections for optimized planar and TiO_2-scaffold devices is shown in Figure 9. The thickness of the active perovskite layers measured from Dektak Profilometer for planar and scaffold device is ≈ 250 nm and 450 nm (TiO_2 + perovskite) respectively.

The incident photon-to-current conversion efficiency (IPCE) spectra of all solar cells shows broad response up to 800 nm, with maximum values close to 92% for the device with mesoporous TiO_2. The higher IPCE values of TiO_2 scaffold $MAPbI_3$ devices can be attributed to the more efficient charge separation, which we attribute to the increased contact area between perovskite and TiO_2. Interestingly, the IPCE is very low in the range from 350 to 400 nm for devices without TiO_2 mesoporous scaffold. A possible explanation is that the light in this region is mainly absorbed by PbI_2 remaining near the compact TiO_2 contact. This PbI_2 could be rich in defects and therefore not generate significant photocurrents.

The power conversion efficiency (PCE) was found to improve for devices prepared at 30 to 60 min. of reaction time, from 1.2 to 4.1 %, see Table 1. While the open-circuit potential (V_{OC}) improved with reaction time, it was rather low with a maximum value of 0.76 V. Short-circuit current densities (J_{SC}) were rather high and increasing with reaction time, up to 21.1 mA cm^{-2}. Fill factor were very low (0.3), seriously limiting solar cell performance. We attribute poor solar cell performance to PbI_2, remaining in the perovskite film, located next to the compact TiO_2 / FTO contact. The PbI_2 conduction band edge is located 0.5 eV above $MAPbI_3$ band edge [32]. It will therefore form a barrier for electron injection from $MAPbI_3$ to the compact TiO_2 layer, which will reduce the solar cell efficiency. In addition, during

formation of large perovskite crystals, pinholes can appear in between. Spiro-OMeTAD can penetrate in these holes, which could lead to shunting in the device. In addition, relative high temperature of 150^{o} C in vapor deposition technique could be the major obstacle for production of high efficiency planar devices [11].

(Figure 10)

(Table 1)

The VASP method has previously been explored for planar thin film $MAPbI_3$ solar cells [15], but it has so far not been used in combination with films on mesoporous TiO_2. We obtained good efficiencies for VASP - prepared $MAPbI_3$ on ms-TiO_2, with a best device PCE of 13.3 % (V_{OC} = 0.92 V and J_{SC} = 22.0 mA cm^{-2}) with reduced hysteresis. The complete conversion of PbI_2 found on mesoporous systems seems to resolve the fill factor problem found for planar devices. Reported I-V curves are scanned from Voc to 0 V. Some hysteresis in I-V curves is found, as reported in detail in Supporting Information. Briefly, in planar devices (Figure S6) the hysteresis was large, while it was rather small in case of TiO_2 scaffold devices (Figure S8). The statistics of 65 solar cells prepared are shown in Figure S10.

Conclusions

The conversion of PbI_2 thin films to $MAPbI_3$ perovskite using the vapor-assisted solution process (VASP) was investigated in detail, using films on glass and on mesoporous TiO_2. The formation of an intermediate $(MAI)_{0.5}(PbI_2)$ phase is proposed, on the basis elemental analysis using XPS, intermediate phase peak shifts in Raman spectroscopy and UV-visible spectroscopy that shows in increasing absorption from 650 to 500 nm, which disappears upon long reaction times. This absorption feature is maintained in samples on mesoporous TiO_2, suggesting that this X-Ray amorphous/non-crystalline phase is stabilized within the scaffold. The 100% volume expansion in the PbI_2 to $MAPbI_3$ conversion may be related to this. Poor solar cell performance of planar VASP prepared devices was ascribed to PbI_2 remaining in the film, forming a barrier between the perovskite layer and the compact TiO_2/ FTO contact. Good performance, with efficiencies upto 13.3%, with negligible hysteresis was obtained for VASP prepared devices on mesoporous TiO_2.

METHODS

Sample preparation Samples were prepared by spin coating 1.3 M PbI_2 solution prepared in DMF / DMSO = 7:3 at 4000 rpm for 30 s, and annealed for 30 minutes at 100^{o} C on a hotplate. The substrates used were microscope glass, FTO-coated glass (TEC 15, Pilkington), either with or without a ≈ 300 nm thick mesoporous TiO_2 layer. The mesoporous TiO_2 layer was prepared by spin coating a diluted TiO_2 paste (Dyesol DSL 30 NR-D) at 3000 rpm for 30 s, followed by annealing at 550°C for 30 min on a hotplate. The PbI_2 spin coated samples were placed in a glass petri dish with MAI powder placed directly on top if the films. The samples were subjected to heat at 150^{o} C using a hotplate for different reaction times. The whole procedure was carried out in a dry box equipped with continuous N_2 gas flow (humidity ≦ 18%).

X-ray diffraction (XRD) was performed with a Siemens diffractometer D5000 using CuKα radiation and Diffrac plus XRD commander software. The instrument was set in "detector scan" mode, and the acquisition was done in θ−2θ mode for every 0.02° increment over the Bragg angle range of 10−60°.

Scanning Electron Microscopy (SEM) was performed on a Zeiss (Gemini 1550) microscope having a field emission (FE) electron source and an in-lens detector for secondary electrons. Top View images were recorded using a high tension of 10kV.

UV-vis-NIR spectra were carried on a Varian Cary 5000 UV-Vis-NIR spectrophotometer in transmission mode. The bare glass substrate was used as reference background. A correction was made for appearance of pinholes for films on glass (this limited the maximum absorbance that could be measured, see supporting information).

Raman spectroscopy measurements were measured with a Renishaw InVia Raman spectrometer with 1 cm^{-1} resolution using a frequency-doubled YAG laser (532 nm) and an 1800 lines/mm grating. A 50 x objective was used and gave a laser spot with 3 - 5 μm diameters with 0.01-1mW intensity on the sample depending on measurement mode. A notch filter was used for the Rayleigh (Plasma) line of the 532 nm laser and a notch filter cutting 10 cm^{-1} into the Stokes part of the spectra. For each sample, 50 spectra were recorded in the range 10 - 400 cm^{-1} with no apparent change in the spectra during the cycles. OMHPs were coated on microscope glass substrates.

Steady-State Emission Measurements were obtained on a Fluorolog-3 instrument (Horiba Jobin Yvon) equipped with double-grating excitation and emission monochromators and a 450-W Xe lamp as a light source. The emission spectra were corrected for the spectral sensitivity of the detection system by using a calibration file of the detector response. Front-face illumination (30° with respect to the incident beam) was used to minimize inner-filter effects.

X-ray photoelectron spectroscopy (XPS) were performed with a Scienta ESCA 300 instrument, using monochromatized AlKα radiation hν =1486.7 eV. The pressure in the analysis chamber was around $1x10^{-8}$ mbar and the electron take off angle was 90°. Quantification was performed on the basis of Scofield's relative sensitivity factors [35] The core peak spectra presented were recorded with a pass energy (Ep) of 150 eV and were binding energy calibrated were energy-calibrated versus the Fermi level at zero binding energy which was determined by measuring a gold plate in electric contact with the sample and setting the Au 4f7/2 core level peak to 84.0 eV. The spectra were intensity calibrated versus the Pb4f core peak if not stated otherwise. Charging and radiation effects were checked for by measuring the specific core level repetitively and was found negligible for all spectra reported in the present investigation.

Fabrication of solar cell devices:

Substrates preparation: A patterned FTO-coated glass (13 Ω/sq, Aldrich) was etched by Zn powder and 2 M HCl diluted in deionized water. Subsequently, the substrates were cleaned with detergent diluted in deionized water, rinsed with deionized water, acetone and ethanol, and dried with clean dry air.

A compact blocking layer of TiO_2 (40 nm, c-TiO_2) was deposited onto fluorine doped SnO_2 (FTO, Pilkington, TEC8) substrate by spray pyrolysis using a 20 mM titanium di-isopropoxide bis (acetylacetonate) solution (Aldrich) at 500°C.

Device Fabrication: The etched FTO substrates with the compact n-type layer of TiO_2 (c-TiO_2). After cooling down, 1.3 M PbI_2 in DMF:DMSO, 7:3 vol. were spin coated on the FTO/c-TiO_2 substrates at 4,000 r.p.m. for 30s, and dried at 100°C for 30 min. Once the PbI_2 substrate is cool to room temperature then is covered with CH_3NH_3I powder in a glass petridish in a confined space, and heated at 150°C for different reaction time. Both the deposition of PbI_2 film and treatment of PbI_2 film in CH_3NH_3I vapor are carried out in dry box equipped with continuous N_2 gas flow and humidity ≦ 18%. After deposition of the perovskite

as mention above, the hole transporter spiro-MeOTAD was deposited by spin-coating at 1500 rpm for 20s as described before [29]. Finally, 150 nm thick silver electrodes were deposited on top of the devices by thermal evaporation at ~10^{-6} bar, through a shadow mask.

Power Conversion Efficiency (PCE): The light source of a solar simulator for measuring the current–voltage (J-V) characteristics was a 300 W solar simulator (Newport) calibrated to a 1000 W m^{-2} light intensity at the 1.5 AM Global condition by a certified silicon solar cell (Fraunhofer ISE). The electrical data were recorded with a computer controlled digital source-meter (Keithley Model 2401) with the scan direction from the open-circuit to the short-circuit at a scan rate of 50 mVs^{-1}. The solar cells were masked during the measurement with a metal mask with a square aperture of 0.125 cm^2.

Incident Photon to Current Conversion Efficiency (IPCE): The IPCE spectra were recorded with a computer-controlled setup comprised of a xenon lamp (Spectral Products, ASB-XE-175), a monochromator (Spectral Products, CM110), a potentiostat (PINE instrument Company, Model AFRDE5) and a lock-in amplifier (SRS830), using white LED bias light. The setup was calibrated with a certified silicon solar cell (Fraunhofer ISE) prior to the measurements. TiO_2 scaffold based as well thin film solar cells were illuminated from the aperture area of 0.125 cm^2 using a black mask. The bias light of 0.08 Sun was applied to solar cells with chopping monochromic light of 25~35 hz frequency while scanning IPCE.

Density Functional Theory Calculations: Density functional theory calculations were performed with Gaussian09 [36] using the hybrid functional B3LYP and the scalar relativistic Stuttgart-Dresden core potentials. The convergence criterion for geometry optimization was set to 10^{-8} Hartrees, and DFT linear response calculations were used in subsequent calculations to obtain the theoretical Raman spectra.

ASSOCIATED CONTENT

Supporting Information

(Word Style "Section_Content"). A brief statement in nonsentence format listing the contents of material supplied as Supporting Information should be included, ending with "This material is available free of charge via the Internet at http://pubs.acs.org." For instructions on what should be included in the Supporting Information as well as how to prepare this material for publication, refer to the journal's Instructions for Authors.

AUTHOR INFORMATION

Corresponding Author

Sagar Motilal Jain, e-mail: sagar.jain@kemi.uu.se

Gerrit Boschloo, e-mail: gerrit.boschloo@kemi.uu.se

Present Addresses

(Word Style "Section Content"). †If an author's address is different than the one given in the affiliation line, this information may be included here.

Author Contributions :

S. M. J prepared samples for characterization, performed XRD, UV-Visible, Photoluminescence, FTIR-ATR, $MAPbI_3$ device fabrications, efficiency measurements, data plotting as well analysis and writing the manuscript; B. P. performed the SEM surface morphology images and XPS spectroscopy measurements, analysis and participated in writing the manuscript; Prof. E. M.J. Johansson participated in discussion and suggestions, BW. P. has assisted in device fabrication process; Prof. H. Rensmo guided the XPS analysis ; Prof. T. Edvinsson performed Resonance Raman measurements, analysis and DFT calculations and edited the manuscript ; Prof. G. Boschloo supervised, guided the project and edited the manuscript.

ACKNOWLEDGMENT

We thank the Swedish Energy Agency, the STandUP for Energy program, the Swedish Research Council (VR), the Göran Gustafsson Foundation, and the Knut and Alice Wallenberg Foundation.

REFERENCES

(1) J. Burschka ; N. Pellet, S. J. Moon, R. H. Baker, P. Gao, M. K. Nazeeruddin, and M. Gratzel, Sequential deposition as a route to high-performance perovskite-sensitized solar cells, Nature, 2013, 499, 316-319

(2) Kim, H.-S.; Lee, C.-R.; Im, J.-H.; Lee, K.-B.; Moehl, T.; Marchioro, A.; Moon, S.-J.; Humphry-Baker, R.; Yum, J.-H.; Moser, J. E, Lead Iodide Perovskite Sensitized All-Solid-State Submicron Thin Film Mesoscopic Solar Cell with Efficiency Exceeding 9%. Sci. Rep. 2012, 2, 591

(3) S. Ryu, J. H. Noh, N. J. Jeon, Y. C. Kim, W. S. Yang, J. W. Seo and S. Il Seok, Voltage output of efficient perovskite solar cells with high open-circuit voltage and fill factor, Energy Environ. Sci., 2014, 7, 2614

(4) M. Liu, M. B. Johnston and H. J. Snaith., Efficient planar heterojunction perovskite solar cells by vapor deposition, Nature, 2013, 501,395.

(5) Glazer, A. M., The Classification of tilted octahedral in perovskites, Acta Cryst. 1972, B28, 3384-3392.

(6) G. E. Eperon, V. M. Burlakov, P. Docampo, A. Goriely, H. J. Snaith, Morphological Control for High Performance, Solution-Processed Planar Heterojunction Perovskite Solar Cells, Advanced Functional Material, 2014, 24 ,151.

(7) M. Saliba, K. W. Tan, H. Sai, D. T. Moore, T. Scott, W. Zhang, L. A. Estroff, U. Wiesner, H. J. Snaith, Influence of Thermal Processing Protocol upon the Crystallization and Photovoltaic Performance of Organic−Inorganic Lead Trihalide Perovskites, J. Phys. Chem. C 2014, 118,17171.

(8) D. Liu, T.L. Kelly, Perovskite solar cells with a planar heterojunction structure prepared using room-temperature solution processing techniques, Nature Photonics, 2014, 8, 133.

(9) W. Li, J. Li, L. Wang, G. Niu, R. Gao, Y. Qiu, Post modification of perovskite sensitized solar cells by aluminum oxide for enhanced performance, J. Mater. Chem. A , 2013, 1, 11735

(10) Ball, J.M.; Lee, M. M.; A.; Snaith, H., Low-temperature processed meso-superstructured to thin-film perovskite solar cells, Energy Environmental Science. 2013, 6, 1739.

(11) Chen CW, Kang HW, Hsiao SY, Yang PF, Chiang KM, Lin HW. Efficient and Uniform Planar-Type Perovskite Solar Cells by Simple Sequential Vacuum Deposition, Adv Mater. 2014 Oct; 26(38):6647-52.

(12) Zhou, H. et al. Interface engineering of highly efficient perovskite solar cells, Science (2014) 345, 542–546.

(13) Xiao, Z. et al. Efficient, high yield perovskite photovoltaic devices grown by interdiffusion of solution-processed precursor stacking layers. Energy Environ. Sci. (2014), **7**, 2619–2623.

(14) Ishihara, T. Optical Properties of PbI-Based Perovskite Structures., J. Luminescence, 1994, 61, 269 – 274.

(15) Qi Chen, Huanping Zhou, Ziruo Hong, Song Luo, Hsin-Sheng Duan, Hsin-Hua Wang, Yongsheng Liu, Gang Li and Yang Yang., Planar Heterojunction Perovskite Solar Cells via Vapor-Assisted Solution Process., J. Am. Chem. Soc. 2014, 136, 622−625.

(16) Stoumpos C. C., Malliakas C. D., Kanatzidis M. G., Semiconducting tin and lead iodide perovskites with organic cations: phase transitions, high mobilities, and near-infrared photoluminescent properties., Inorganic Chemistry, 2013, 52, 9019 - 9038.

(17) Yani Chen, Yixin Zhao, and Ziqi Liang, Non-Thermal Annealing Fabrication of Efficient Planar Perovskite Solar Cells with Inclusion of NH_4Cl, Chem. Mater. 2015, 27, 1448-1451

(18) Yani Chen , Yixin Zhao and Ziqi Liang **,** Nonvolatile chlorinated additives adversely influence $CH_3NH_3PbI_3$ based planar solar cells, J. Mater. Chem. A, 2015, **3**, 9137-9140

(19) Cullity, B. D., Elements of X-ray Diffractions; Addition-Wesley: London, 1959; p 99

(20) Li, L.; Fang, L.; Chen, X. M.; Liu, J.; Yang, F. F.; Li, Q. J.; Liu, G. B.; Feng, S., Influence of oxygen argon ratio on the structural, electrical, optical and thermoelectrical properties of Al-doped ZnO thin films J. Physica E 2008, 41, 169 – 174

(21) Ostwald, W. The Formation and Changes of Solids. Z. Phys. Chem. 1897, 289 - 330.

(22) Zhou, Z ; Wang, Z ; Zhou, Y; Pang, S; Wang, D; Xu, H; Liu, Z ; Padture, N, P, ; and Cui, G; Methylamine-Gas-Induced Defect-Healing Behavior of $CH_3NH_3PbI_3$. Thin Films for Perovskite Solar Cells, Angew. Chem. Int. Ed. 2015, 54, 9705 –9709

(23) Joshua J. Choi, Xiaohao Yang, Zachariah M. Norman, Simon J. L. Billinge and Jonathan S. Owen, Structure of Methylammonium Lead Iodide Within Mesoporous Titanium Dioxide: Active Material in High-Performance Perovskite Solar Cells, Nano Lett., 2014, 14, 127 - 133.

(24) Noh J. H.; Im S. H.; Heo J. H. ; Mandal T. N.; Seok S. I. ; Chemical Management for Colorful, efficient and stable Inorganic – Organic hybrid nanostructured solar cells, Nano Lett., 2013, 13 (4), 1764 - 1769.

(25) Saidaminov, M, I ; Abdelhady Ahmed L.; Murali Banavoth; Alarousu, Erkki ; Burlakov, Victor M.; Peng, Wei; Dursun, Ibrahim; Wang, Lingfei ; He, Yao ; Maculan, Giacomo; Goriely, Alain; Wu, Tom; Mohammed Omar F.; & Bakr Osman M., High-quality bulk hybrid perovskite single crystals within minutes by inverse temperature crystallization, Nature Communications **6**, Article number:7586

(26) Dong Shi, Valerio Adinolfi, Riccardo Comin, Mingjian Yuan, Erkki Alarousu, Andrei Buin, Yin Chen, Sjoerd Hoogland, Alexander Rothenberger, Khabiboulakh Katsiev, Yaroslav Losovyj, Xin Zhang, Peter A. Dowben, Omar F. Mohammed,1 Edward H. Sargent, Osman M. Bakr, Low

trap-state density and long carrier diffusion in organolead trihalide perovskite single crystals, Science (2015), 347 6221, 519-522.

(27) Qi Chen, Huanping Zhou, Tze-bin Song, Song Luo, Ziruo Hong, Hsin-Sheng Duan, Letian Dou, Yongsheng Liu, Yang Yang., Controllable self-induced passivation of hybrid lead iodide perovskites toward high performance solar cells, Nano Lett. (2014), 14, 4158−4163.

(28) Byung-wook Park, Sagar M. Jain, Xiaoliang Zhang, Anders Hagfeldt , Gerrit Boschloo, and Tomas Edvinsson., Resonance Raman and excitation energy dependent charge transfer mechanism in halide-substituted hybrid perovskite solar cells, ACS Nano, 2015, 9 (2), 2088 – 2101.

(29) Claudio Quarti, Giulia Grancini, Edoardo Mosconi, Paola Bruno, James M. Ball, Michael M. Lee, Henry J. Snaith, Annamaria Petrozza and Filippo De Angelis, The Raman Spectrum of the $CH_3NH_3PbI_3$ Hybrid Perovskite: Interplay of Theory and Experiment. J. Phys. Chem. Lett. 2014, 5, 279−284.

(30) A. Maaej , M. Bahri , Y. Abid , N. Jaidane , Z. B. Lakhdar & A. Lautié, Raman study of low temperature phase transitions in the cubic perovskite $CH_3NH_3PbCI_3$, Phase Transitions, (1998) ,64:4, 179-190.

(31) R. Lindblad, N. K. Jena, B. Philippe, J. Oscarsson, D. Bi, A. Lindblad, S. Mandal, B. Pal, D. D. Sarma, O. Karis, H. Siegbahn, E. M. J. Johansson, M. Odelius, H. Rensmo, Electronic Structure of $CH_3NH_3PbX_3$ Perovskites: Dependence on the Halide Moiety, J. Phys. Chem. C, 2015, 119, 1818 – 1825.

(32) R. Lindblad, D. Bi, B.-w. Park, J. Oscarsson, M. Gorgoi, H. Siegbahn, M. Odelius, E. M. J. Johansson, H. Rensmo, , J. Phys. Chem. Lett, 2014, *5*, 648 – 653.

(33) B. Philippe, B.-w. Park, R. Lindblad, J. Oscarsson, S. Ahmadi, E. M. J. Johansson and H. Rensmo Chemical and Electronic Structure Characterization of Lead Halide Perovskites and Stability Behavior under Different Exposures: A Photoelectron Spectroscopy Investigation, Chem. Mater., 2015, 27, 1720 – 1731.

(34) Zhaoning Song, Suneth C. Watthage, Adam B. Phillips, Brandon L. Tompkins, Randy J. Ellingson and Michael J. Heben., Impact of Processing Temperature and Composition on the Formation of Methylammonium Lead Iodide Perovskites, Chem. Mater. 2015, 27, 4612−4619

(35) Scofield, J. H., Hartree-Slater subshell photoionization cross-sections at 1254 and 1487 eV, J. Electron Spectrosc. Relat. Phenom. 1976, 8, 129 -137

(36) Frisch, M. J.; Trucks, G. W.;Schlegel, H. B.; Scuseria, G. E.; Robb, M. A.; Cheeseman, J. R.;Scalmani, G.; Barone, V.; Mennucci, B.; Petersson, G. A. et al. Gaussian 09, Revision A.02; Gaussian, Inc.: Wallingford, CT, 2009

(37) Nam Joong Jeon, Jun Hong Noh, Young Chan Kim, Woon Seok Yang, Seungchan Ryu & Sang Il Seok . Solvent engineering for high-performance inorganic-organic hybrid perovskite solar cells., Nature Materials, (2014),13, 897–903.

Figure Captions

Figure 1. Evolution of the XRD patterns as a function of the reaction time of MAI with PbI_2 thin films, (a) on plain glass substrate, (b) on a glass with mesoporous TiO_2 scaffold. Symbols indicate diffraction peaks of PbI_2 (*), MAI (+), TiO_2 (x) and $MAPbI_3$ perovskite (o). (c,d) Schematic illustration of the $MAPbI_3$ formation on a glass substrate without and with mesoporous TiO_2 scaffold layer, respectively. The yellow-green lines on surface of $MAPbI_3$ represent grain boundaries.

Figure 2. Top-view SEM pictures of the PbI_2 layer at t=0 min and evolution after reaction with MAI vapors (a) on FTO after 0, 10, 30, 45 and 60 min and (b) on mesoporous TiO_2 /FTO after 0, 10, 20 and 30 min. PbI_2 are presented with two difference magnifications (1 μm and 0.2 μm scales, horizontal bars), while the sample exposed to MAI are with the same magnification (1 μm scale, horizontal bars).

Figure 3. UV-Visible spectra for the sequential formation of $MAPbI_3$ from PbI_2 as a function of reaction time with MAI vapors for different reaction times. (a) Films on glass substrate. (b) Films on mesoporous-TiO_2/ glass substrate; Schematic pictures and photographs of the corresponding samples are presented as *insets*.

Figure 4. Photoluminescence spectra of PbI_2 and $MAPbI_3$ films on glass substrates. Excitation wavelength 420 nm.

Figure 5. Resonance Raman spectroscopy of PbI_2 prepared on (a) glass and (b) glass/mesoporos TiO_2 and stepwise formation of $MAPbI_3$, as a function of reaction time with MAI.

Figure 6. Fundamental vibration modes of a PbI_6 octahedron with Oh symmetry (top) and MA^+ cation perturbed vibration modes (middle) and theoretical Raman spectrum of a $(MAPbI_3)_4$ cluster performed with linear response DFT with B3LYP using the scalar relativistic Stuttgart-Dresden effective core potentials (bottom).

Figure 7. X-ray photoelectron spectroscopy: (a) I4d/Pb5d, (b) N1s and (c) C1s core level spectra of the PbI_2 layer and after a reaction time of 10, 30, 45 and 60 with MAI. The spectra in (b) and (c) were intensity normalized to the $Pb4f_{7/2}$ core level for a better comparison.

Figure 8. Valence level spectra of the PbI_2 layer and after a reaction time of 10, 30, 45 and 60 min with MAI. The spectra were intensity normalized to the $Pb4f_{7/2}$ core level for a better comparison.

Figure 9. SEM Cross-section images for the optimized $MAPbI_3$ perovskite devices (a) $MAPbI_3$ Thin film device cross-section (a1) Cross-section between FTO-$MAPbI_3$, (a2) lateral FTO-$MAPbI_3$ cross-section - indicating surface coverage. (b) $MAPbI_3$ TiO_2-mesoporous device crossection, (b1) $MAPbI_3$ capping layer - intersection cross-section between TiO_2-scaffold and $MAPbI_3$ capping layer, (b2) Surface SEM image of $MAPbI_3$ capping layer – indicating surface coverage.

Figure 10. Selected $MAPbI_3$ solar cell results (a) J-V curves and (b) IPCE curves of thin film $MAPbI_3$ solar cell devices formed using 30, 45 and 60 minute reaction time. For comparison results of a TiO_2 scaffold device (optimized 30 minutes reaction time) is shown (c) Schematic representation of $MAPbI_3$ formation on different reaction time for thin film $MAPbI_3$ and $MAPbI_3$/mesoporous devices.

Table 1. Photovoltaic performance at 1000 W m^{-2} (AM1.5G) of planar thin film $MAPbI_3$ devices with different VASP reaction times and comparison with VASP device prepared on mesoporous TiO_2 scaffold.

Reaction time (minutes)	V_{OC} **(V)**	J_{SC} **(mAcm^{-2})**	***FF***	***PCE* (%)**
30	0.32	-16.0	0.23	1.3
45	0.57	-19.7	0.30	3.3
60	0.76	-21.1	0.28	4.4
30_scaffold	0.91	-22.0	0.65	13.3

Figure 1.

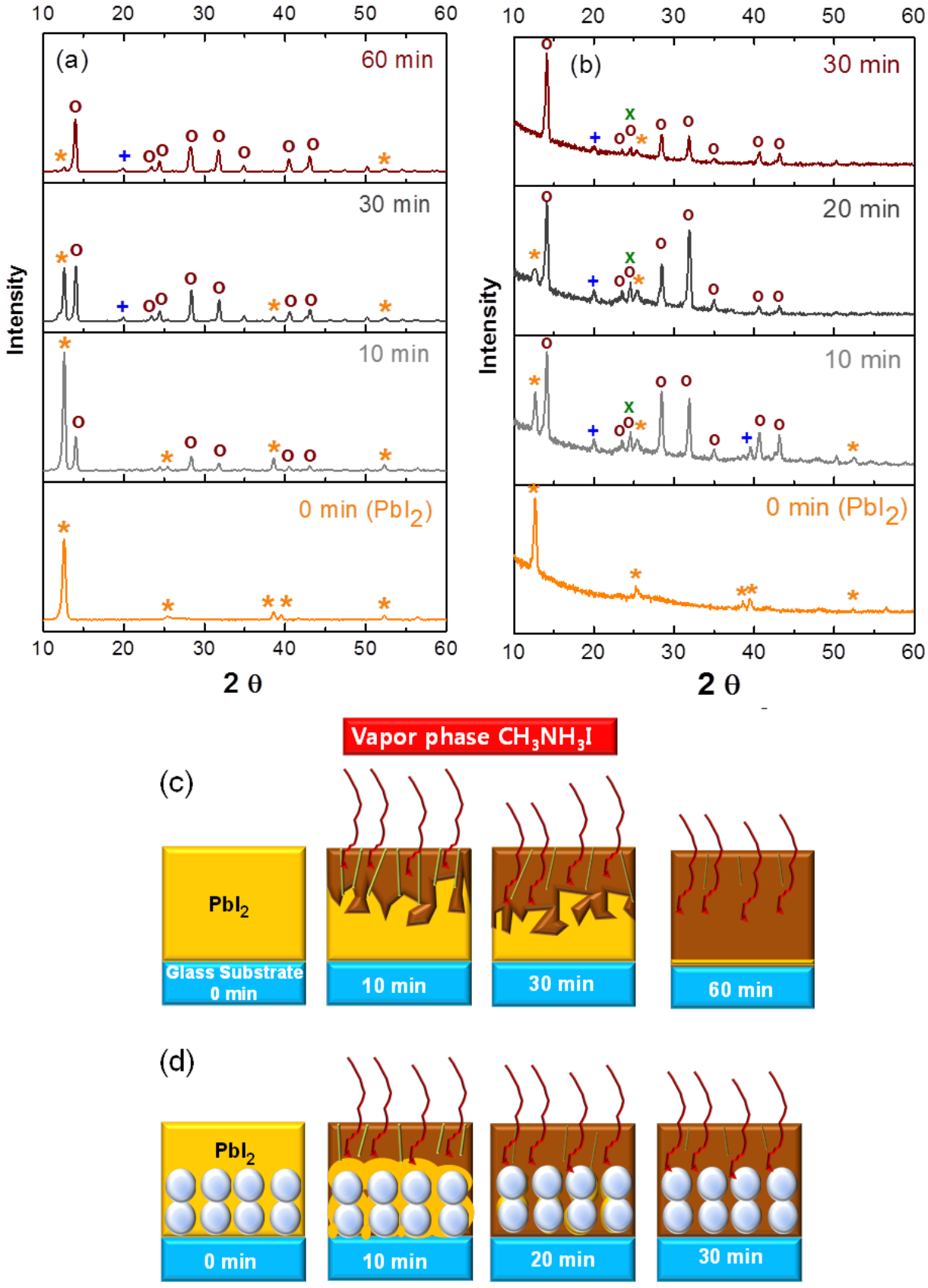

Figure 2.

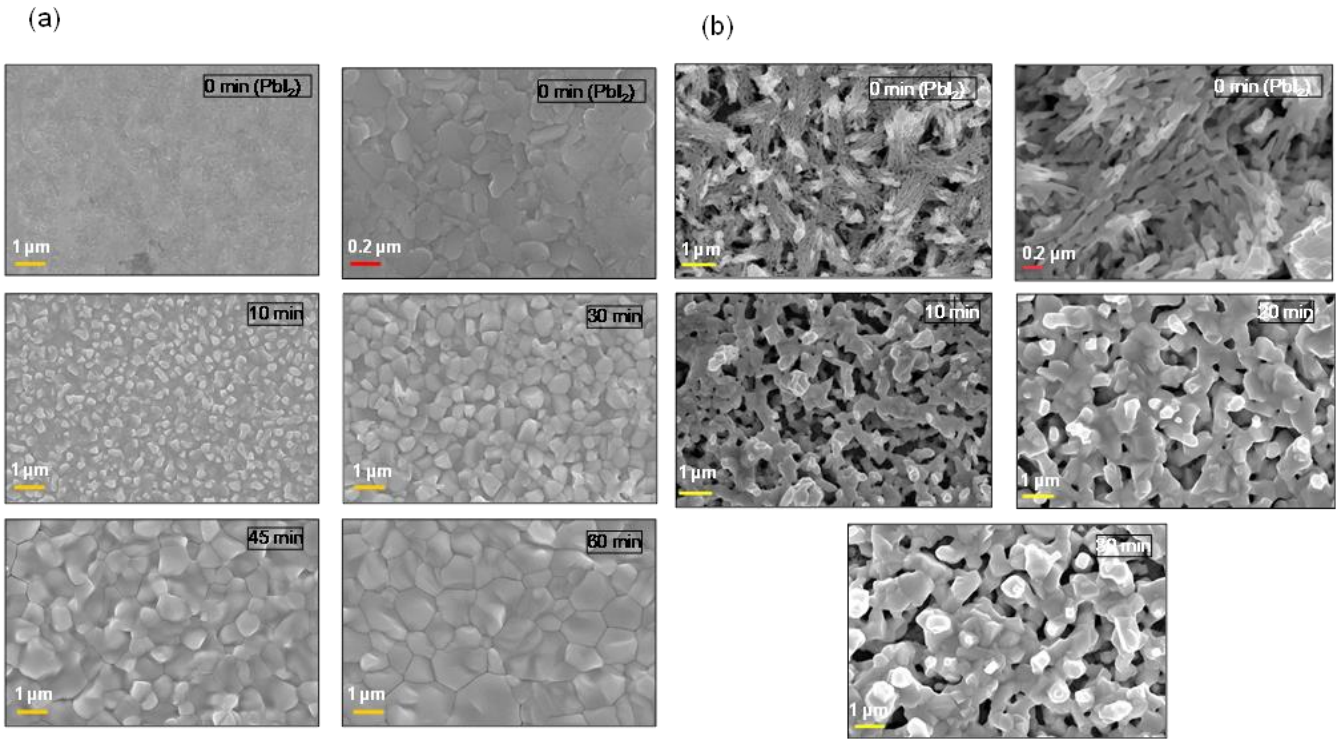

Figure 3.

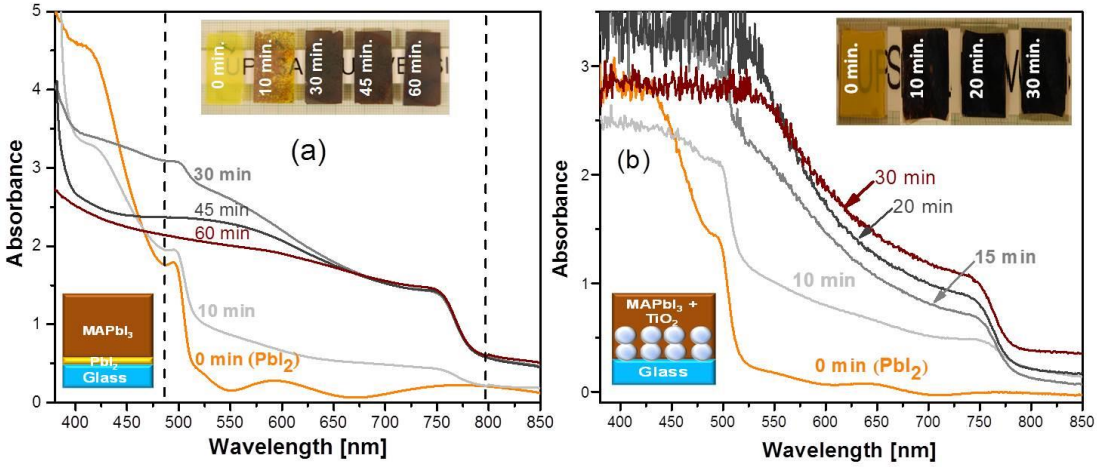

Figure 4.

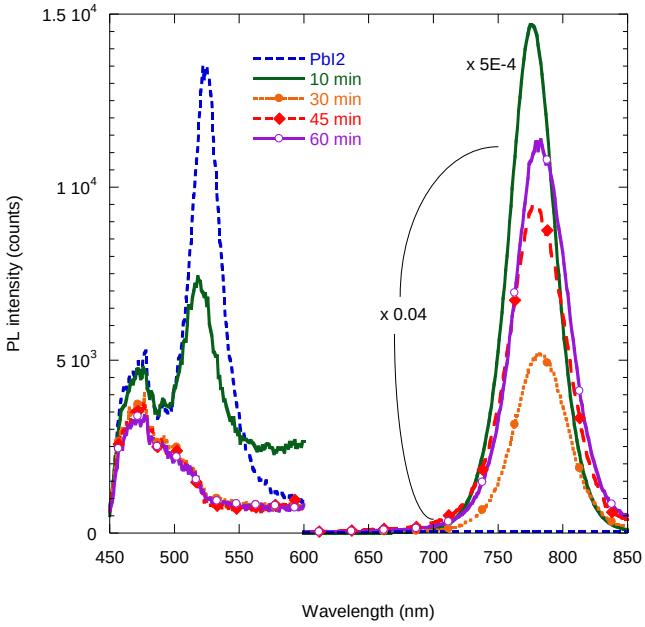

Figure 5.

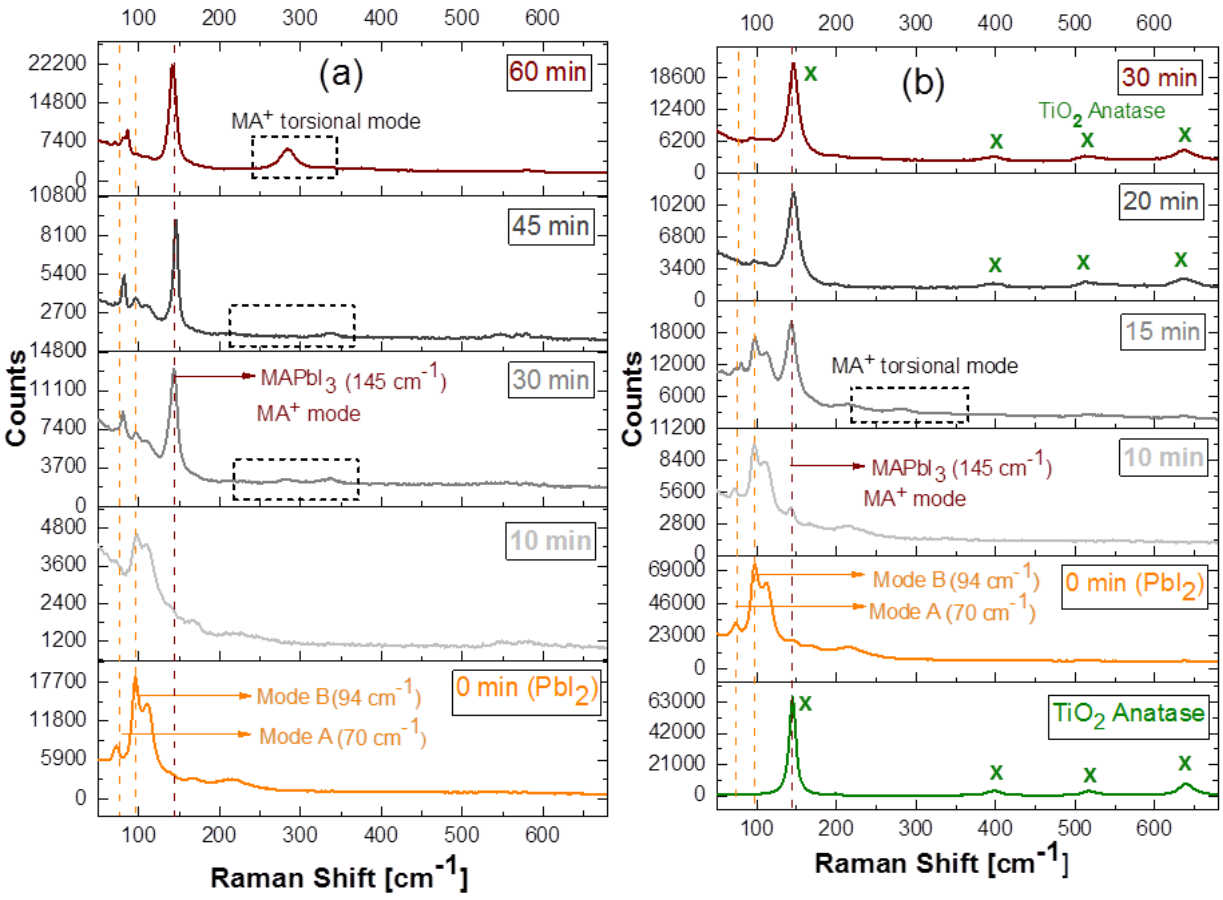

Figure 6.

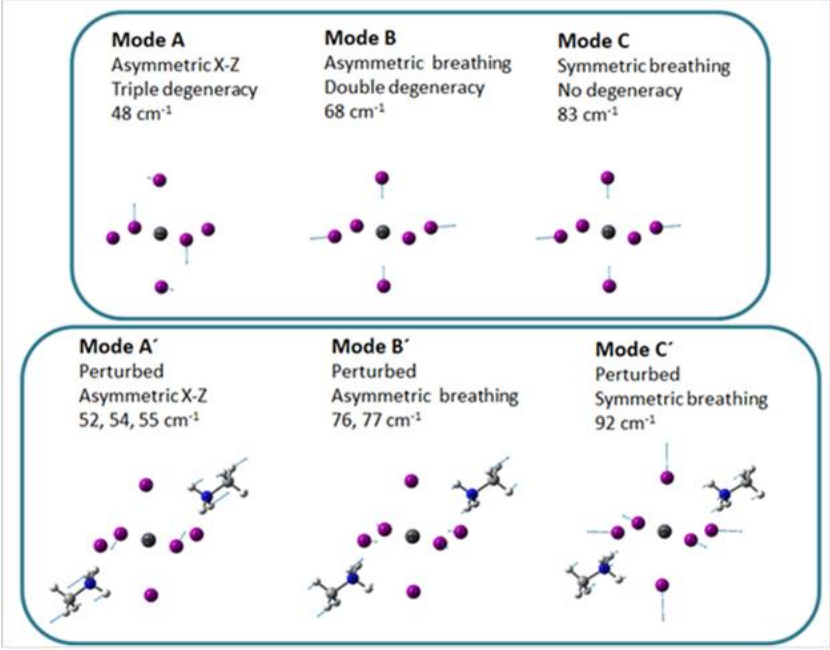

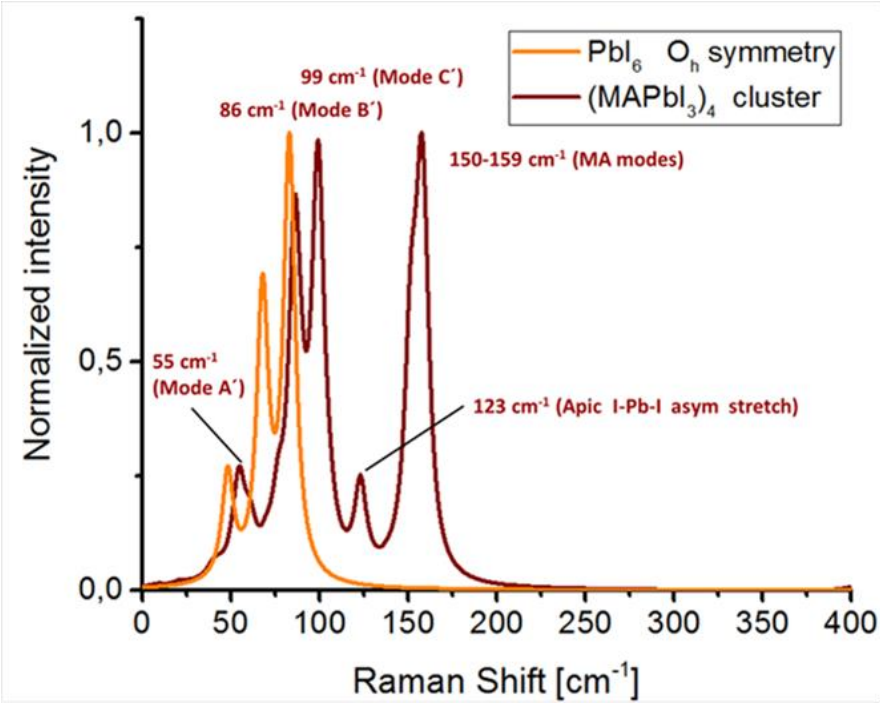

Figure 7.

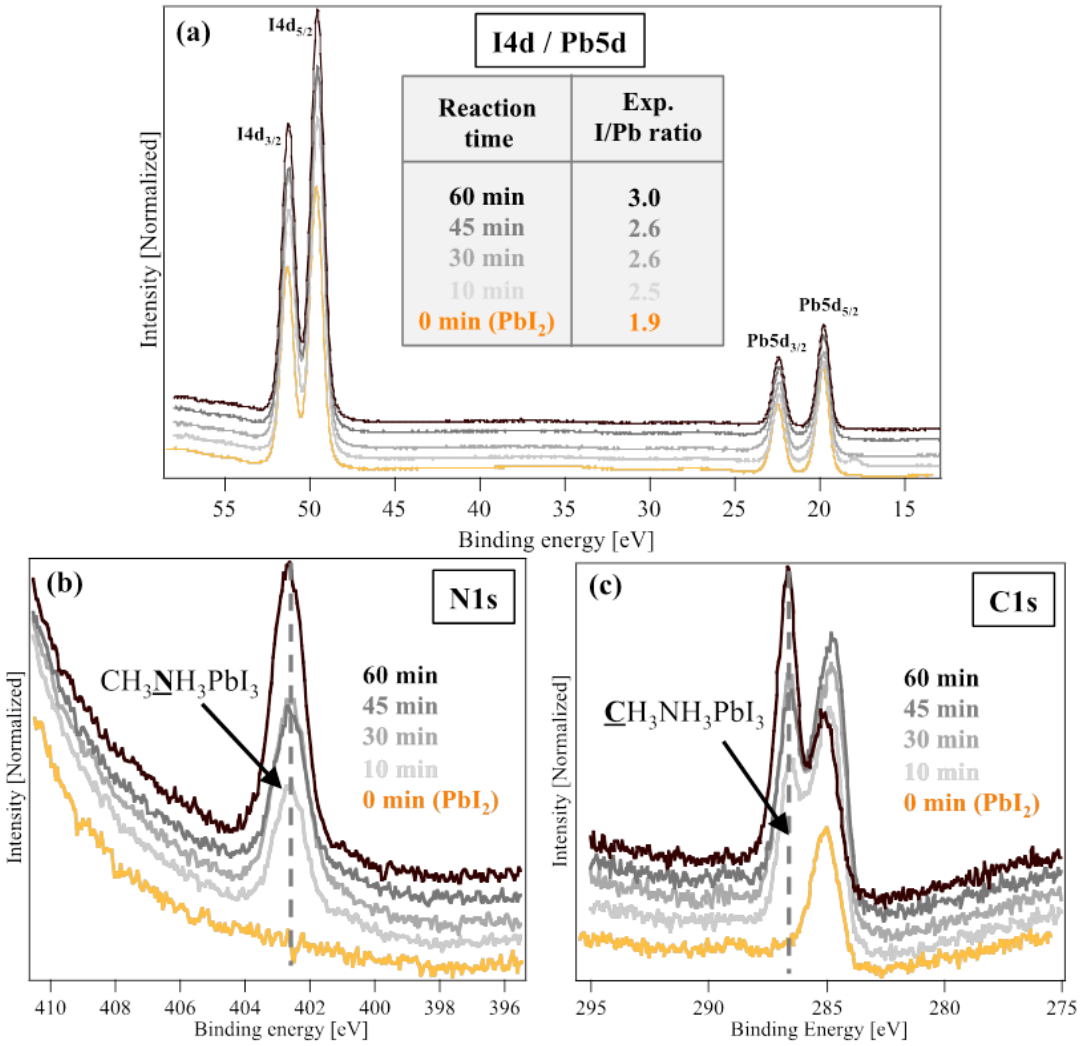

Figure 8.

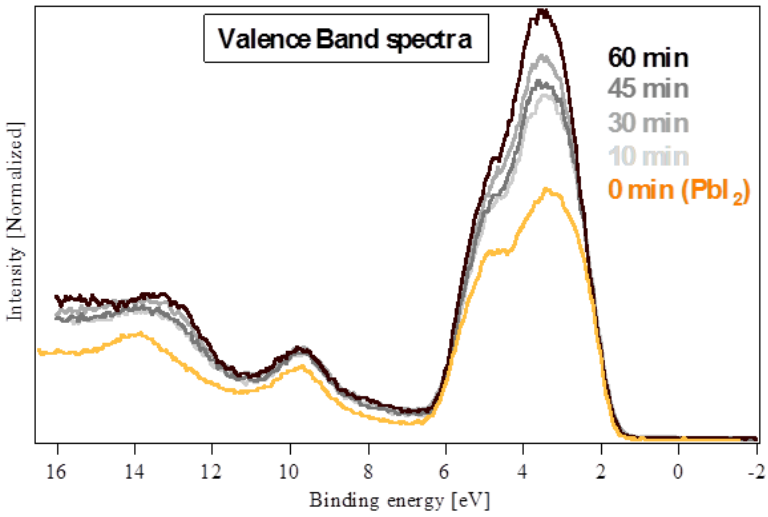

Figure 9.

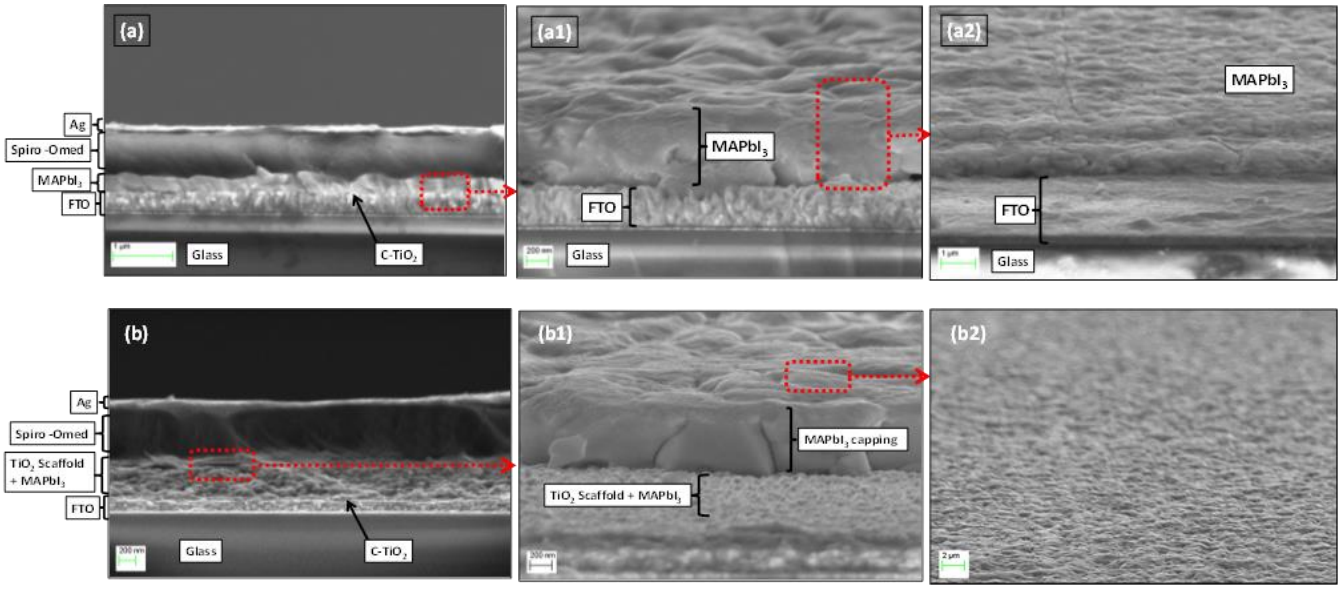

Figure 10.

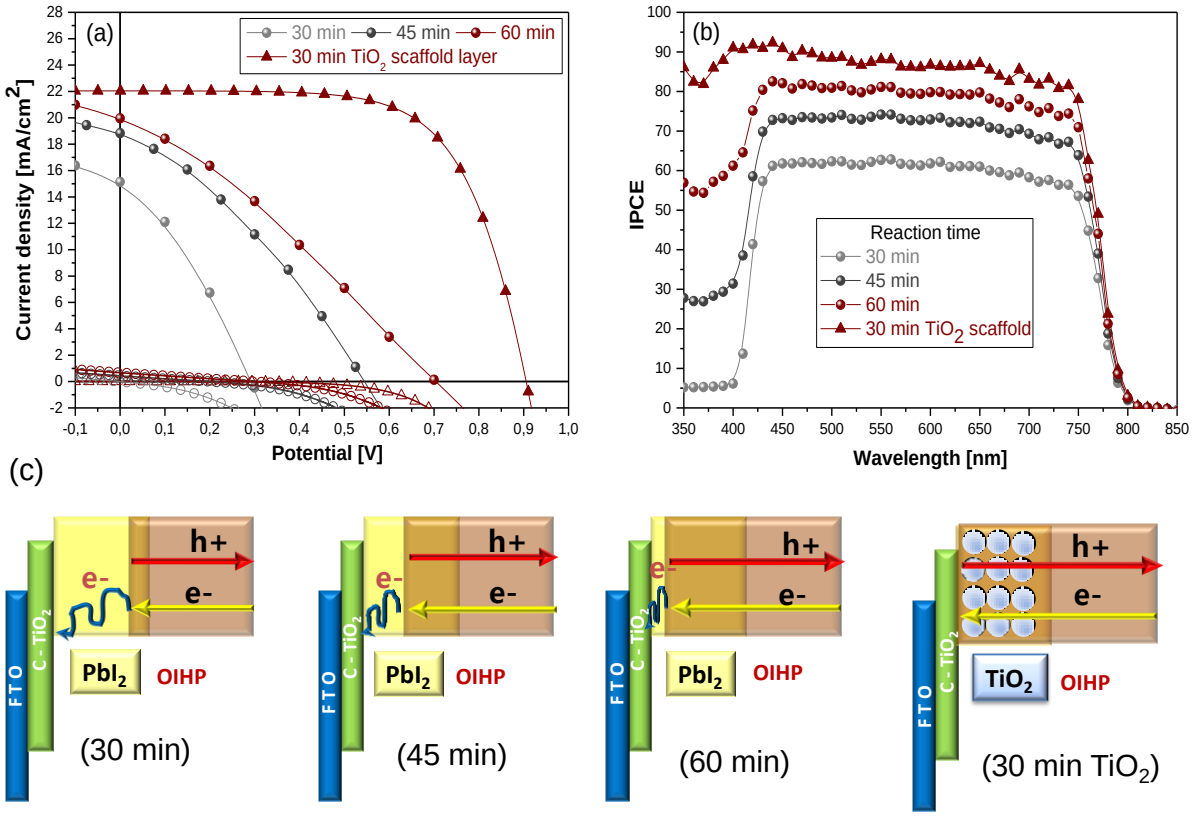

TOC Figure :-